INSTITUTE OF PHYSICS PUBLISHING JOURNAL OF PHYSICS D: APPLIED PHYSICS
J. Phys. D: Appl. Phys. **36** (2003) R39–R51 PII: S0022-3727(03)30149-4

TOPICAL REVIEW

Micromechanical instruments for ferromagnetic measurements

John Moreland

National Institute of Standards and Technology, Boulder, CO 80305, USA

Received 3 October 2002
Published 14 February 2003
Online at stacks.iop.org/JPhysD/36/R39

Abstract

I review some of the novel methods for measuring ferromagnetic properties of thin films based on micromechanical magnetometers and put them into context relative to current research on nanomagnetism. Measurements rely on the detection of mechanical forces or torques on thin films deposited onto microcantilevers. Displacements of the cantilever are detected by optical methods similar to those developed for atomic force microscopy. High sensitivities are achieved by integrating the sample with the detector, allowing magnetic measurements of samples with a total magnetic moment smaller than that detectable with conventional magnetometers. Cantilevers with low spring constants and high mechanical Q are essential for these measurements. Sensitivities better than $10^5\ \mu_B$ are possible at room temperature with the potential for single spin detection below 1 K, where the thermomechanical noise of micromechanical sensors is substantially reduced.

Nomenclature

$\hbar$	Planck's constant
e	electron charge
m_e	electron mass
γ_e	electronic gyromagnetic ratio
μ_0	permeability of free space
μ_B	electron magnetic moment (Bohr magneton)
μ_p	proton magnetic moment
μ_n	neutron magnetic moment
V	volume
M	magnetization
M_s	saturation magnetization
M_{eff}	effective magnetization
M_z	z-component of the magnetization
M_x	x-component of the magnetization
M_y	y-component of the magnetization
m	magnetic moment
F	force
Γ	torque
Γ_{esr}	ESR torque absorption at resonance
Γ_{fmr}	FMR torque absorption at resonance
P	power absorbed
P_{esr}	ESR power absorbed at resonance
P_{fmr}	FMR power absorbed at resonance
H	magnetic field strength
H_1	microwave magnetic field
h_x	x-component of the microwave field
h_y	y-component of the microwave field
H_Γ	torque field
H_0	bias (sweep) field
H_{fmr}	FMR resonance field
B	magnetic flux density
φ	magnetic flux
ω_1, f_1	microwave frequency
α	FMR Gilbert damping factor
χ''_{fmr}	imaginary part of the magnetic susceptibility at FMR resonance
N	number of microwave photons
t_f	magnetic film thickness
K_s	magnetic surface anisotropy energy
δ	skin depth
ρ	resistivity
μ	permeability
z	cantilever deflection distance
θ	cantilever torsion angle

k	cantilever deflection spring constant
k_θ	cantilever torsion spring constant
w	cantilever width
l	cantilever length
t	cantilever thickness
f_0	cantilever resonance frequency
Q	cantilever mechanical Q
E	Young's modulus
n	Poison ratio
γ	thermal expansion coefficient
λ	thermal conductivity
k_B	Bolztmann's constant
T	temperature

1. Introduction

The characterization of thin magnetic films, patterned recording media, and nanometre-scale magnetic devices has proven to be a challenge for conventional magnetometers. The limitation on the dynamic range of magnetic sensors used in these instruments is fundamentally understood by comparing the energy necessary to excite the sensor relative to the energy necessary to excite the specimen for measurement purposes. Conventional magnetometers are designed for measurements of large specimens and therefore have a relatively low signal-to-noise ratio (SNR) for small specimens. Sensitivity can be improved tremendously by integrating specimens with the measurement sensor using microfabrication methods. In many cases, one can achieve a more favourable energy ratio without sacrificing signal. Micromechanical magnetometers with integrated samples can provide a cost-effective solution since this technology is based on conventional silicon microfabrication techniques. For example, arrays of micromechanical sensors offer possibilities for high-throughput analysis based on combinatorial methods for developing new thin-film materials for nanometre-scale devices.

In this paper, I describe several magnetometers based on microelectromechanical systems (MEMS) for measuring magnetic forces and torques on specimens deposited onto microscopic structures. Magnetomechanical phenomena have been the basis for many physics discoveries over the last 140 years. Consider, for example, the definition for the electronic gyromagnetic constant for magnetic material, $\gamma_e = m/L$, where m and L are the magnetic moment and internal angular momentum of the magnet, respectively. Requiring that γ_e be a constant, presumably related to the fundamental origins of magnetism in an object, indicates that mechanical and magnetic properties measurements are intimately related. In fact, many of the fundamental constants as we know them today depend on measurements of magnetic properties, which are related to the motion of elementary particles or atomic state transitions induced by electromagnetic fields. Even the ampere is described in terms of magnetic forces: the ampere is that constant current which, if maintained in two straight parallel conductors of infinite length, of negligible circular cross-section, and placed 1 m apart in vacuum, would produce between these conductors a force equal to 2×10^{-7} newton per metre of length [1]. Note that the effect of this definition is to fix the magnetic constant (permeability of vacuum) at exactly $\mu_0 = 4\pi \times 10^{-7}\,\mathrm{H\,m^{-1}}$.

Measurements of the fundamental constants related to magnetic moments (μ_B, μ_p, μ_n, and the corresponding gyromagnetic ratios) are performed on isolated particles or on systems of non-interacting particles to close approximation. This greatly simplifies the physical interpretation of the measurements. There has also been a great deal of work on precision magnetomechanical measurements of macroscopic systems where the total magnetic moment of a large number of interacting particles is considered and the atomic level magnetism is determined simply by dividing measured properties by the number of magnetic atoms or molecules in the sample. It is these experiments that we wish to focus on in this paper, particularly instrumentation developed for ferromagnetic materials.

Magnetomechanical effects on macroscopic systems can be generally categorized as a force or torque acting on an object. If the system is dissipative then heat will also be generated and can be measured and correlated to applied forces or torques. I further limit the scope of this paper to measurements of the magnetic moment of a specimen made using instruments designed to measure torque $\boldsymbol{\Gamma} = \mu_0 \boldsymbol{m} \times \boldsymbol{H}$ and force $\boldsymbol{F} = \boldsymbol{\nabla}(\boldsymbol{m} \cdot \boldsymbol{B}) = \mu_0(\boldsymbol{m} \cdot \boldsymbol{\nabla})\boldsymbol{H}$ (in the absence of currents). So, in principle, if one knows $\boldsymbol{m}$ then one can determine $\boldsymbol{H}$ or $\boldsymbol{\nabla H}$ from measurements of $\boldsymbol{\Gamma}$ or $\boldsymbol{F}$. Conversely, $\boldsymbol{m}$ can be determined if $\boldsymbol{H}$ or $\boldsymbol{\nabla H}$ are known.

2. Background

2.1. Torque magnetometers

Some of the first quantitative magnetism experiments relied on measurements of torque due to fixed moments reacting to an applied field. Torque measurements require that the magnetic torque on a specimen react against mechanical deformations of a torque spring through magnetic anisotropies of the sample. Torque magnetometers are generally based on a torsional pendulum attached to a specimen suspended between the poles of a rotating dipole magnet [2]. The specimen is deposited or glued to the pendulum and the rotation is measured with an optical lever or a capacitance sensor. Torque magnetometers are very sensitive and widely used to measure magnetic moments and anisotropies, with many improvements having been made over the last century. Instrumentation development is still on going, with a great deal of work being focused on micromechanical torque sensors made with silicon micromachining techniques. Notable applications of MEMS torque magnetometers include the de Hass–van Alphen effect [3], superconductor vortex dynamics [4, 5], two-dimensional electron gas measurements [6–8], CMOS integrated gaussmeter sensors [9], and the measurements of thin-film moments and anisotropies [10–13].

An interesting early observation of magnetic torque phenomena lies in the equivalency of magnetic moment and angular momentum. It was Maxwell who first advanced the concept of 'hidden angular momentum' in magnets. Later, several researchers performed experiments related to the direct measurement of the 'magnetomechanical ratio' (or more familiarly the electronic gyromagnetic constant γ_e).

In particular, the Barnett effect, whereby the magnetization can be changed by sample rotation, or conversely, the Einstein–de Hass effect, whereby sample rotation is induced by changes in magnetization. These measurements led to the first observations of the deviation of the gyromagnetic constant from the value $\gamma_e = -e/2m_e$ in ferromagnetic materials due to spin–orbit coupling [14].

2.2. Field gradient magnetometers

Another way to measure $\boldsymbol{m}$ quantitatively is to immerse a specimen in a uniform field gradient as discussed above, thus generating a force. Two methods have been developed that work this way: (1) the Faraday method [15] for measuring susceptibility simply measures the force on a sample with a mechanical balance, and (2) the alternating field gradient magnetometer (AGM) [16] where an oscillating magnetic field gradient induces an alternating force on the specimen mounted on a flexible reed and as a result the specimen vibrates. The mechanical quality factor of the AGM vibrating system near resonance is used to amplify the signal. It is also worth mentioning the vibrating sample magnetometer (VSM) [17] where a sample is vibrated in the vicinity of a set of pick-up coils. The flux change caused by the moving magnetic sample induces a voltage across the terminals of the pick-up coils that is proportional to the magnetization of the specimen. Although the VSM and AGM can be thought of as the inverses of each other, where the VSM measures $\mathrm{d}\varphi/\mathrm{d}t$ due to the motion of the sample and the AGM uses changes in $\mathrm{d}\varphi/\mathrm{d}t$ to move the sample, strictly speaking, the VSM does not provide a 'mechanical measurement' of magnetic properties since it does not measure force or torque.

As is the case for torque measurements, force measurements of magnetic properties have also benefited from microfabrication of sensors. AGM performance has been improved substantially by using a silicon microcantilever as the vibrating reed [18–20]. The ultimate application has been the development of atomic force microscopy (AFM) [21] and one of its many derivatives, magnetic force microscopy (MFM) [22], with 10 nm resolution and force sensitivities as low as 10^{-15} N [23]. Unfortunately, quantitative measurements of either field gradients or tip magnetization are very difficult at the nanoscale and thus it is challenging to make MFM a quantitative technique.

2.3. Mechanical detection of magnetic resonance

2.3.1. Angular-momentum absorption. Magnetic resonance spectroscopy is typically performed by placing a specimen in a microwave resonant cavity. When an applied background field is adjusted to match magnetic resonance conditions, the spins in the sample precess, causing a change in the Q of the microwave cavity due to power absorption. Magnetic resonance also generates internal mechanical torque. Torque induced by electron spin resonance (ESR) was first measured using a torque magnetometer [24–26]. In the analysis of ESR torque it is assumed that circularly polarized photons with frequencies matching the spin precession are absorbed. Under this assumption, each absorbed microwave photon with frequency ω_1 contributes quanta $\hbar\omega_1$ of energy and $\hbar$ of angular momentum so that the absorbed power P_{esr} is directly related to the torque by $P_{esr} = \omega_1 \Gamma_{esr}$. This technique has recently been demonstrated with microcantilevers replacing larger scale torque magnetometers [27]. We have extended the concept even further to ferromagnetic resonance (FMR), which will be discussed in some detail in this paper.

2.3.2. Magnetic resonance force microscopy (MRFM). MRFM is an adaptation of MFM based on the magnetic dipole interactions of a scanning cantilever tip and the sample. It is a force measurement method where the net magnetic moment of the specimen is modulated by bringing the spins in the sample in and out of resonance [28]. This gives rise to a modulated force on the cantilever, which is typically applied at the resonance frequency of the cantilever to improve SNR. In principle, at low temperatures (100 mK) this technique can detect a single electron spin (one Bohr magneton μ_B). This technique has been applied to NMR [29], ESR [30], and FMR [31].

2.3.3. Torque mode FMR. It is also possible to perform torque measurements of magnetic resonance where again the net magnetic moment of the sample is modulated in a manner similar to that of MRFM. There is the additional requirement that the specimen have magnetic anisotropy for torque to be transmitted to a cantilever so this method is particularly useful for FMR of thin films (see discussions later).

2.3.4. Calorimetric FMR. This technique is based on the bimaterial effect whereby a cantilever comprised of two thin films with different thermal expansion coefficient bends upon heating. Under magnetic resonance conditions there is a peak in the absorbed microwave power and thus a peak in the deflection of the cantilever. Strictly speaking, this is not a 'mechanical measurement' but it may be useful for quantitative measurements (see discussions later).

3. Nanomagnetism measurement challenges

New ways are being developed to measure the magnetic properties of individual nanometre-scale particles. The ability to measure one particle as opposed to an array or clump of particles will lead to a better understanding of quantum size effects. Magnetic properties are governed by the complex interplay of inter- and intra-particle interactions that can be difficult to separate and understand. By measuring one particle, statistical variations in parameters, such as particle size and spacing in a group of particles, are eliminated from the analysis of the data. Fundamental studies of surface and interface magnetism can also benefit from the development of more sensitive magnetometers. Magnetic moment sensitivities corresponding to a fraction of a monolayer film thickness are required for these studies to measure subtle changes in the magnetic moment of thin films and mutilayers as a function of applied field. Some of the current metrology challenges are discussed briefly below.

3.1. New recording media for hard disk drives

In efforts to circumvent the thermal-stability recording limit [32], a great deal of research has gone into developing new types of recording media. Media with tailored grain structure, perpendicular media, artificial antiferromagnetically coupled (AFC) media, self-assembled media, and patterned media have been investigated. Each technology faces different materials problems that affect the nanometre-scale magnetic domain structure and spin dynamics of the media. Media with tailored grain structure require the development of underlayers and seed layers for controlling grain size and orientation [33]. Perpendicular media require the development of a keeper layer to provide a return flux path for the monopole recording head [34]. AFC media require exchanged-coupled films tailored for high-density longitudinal recording [35]. Self-ordered media require development of chemical pathways that lead to control of size, inter-particle interaction and particle ordering [36, 37]. Patterned media require the development of isolated, thermally stable bits smaller than 25 nm and separated by less than 25 nm defined by lithographic or chemical means [38].

3.2. Magnetic random access memory (MRAM)

MRAM technology has advanced greatly with the development of spin-valve and magnetic tunnel junction (MTJ) sensors [39, 40]. MRAM elements less than $1\,\mu$m in size are now being developed for high-density element arrays. Here again, thermally stable domain configuration is a problem as well as MRAM element shape, which determine the micromagnetics of switching between stable configurations.

3.3. Magnetoelectronics

The main idea in magnetoelectronics [41–43] is to observe and manipulate spin accumulation in ferromagnetic semiconductors. It is likely that the best way to do this is to look at nanometre-scale effects by integrating spin-valve or MTJ sensors with magnetic semiconductor devices. The idea is to pump electron spin magnetism (or equivalently, angular momentum) around an electronic circuit in packets of less than $1000\,\mu_{\mathrm{B}}$.

3.4. Interface magnetism

The discovery of giant magnetoresistance (GMR) in thin-film multilayers and the subsequent development of spin-valve sensors have led to a new appreciation of magnetic phenomena at the nanometre scale [44]. Seldom has a basic physics discovery been transferred from the lab to commercial products so quickly as in the case of the GMR effect and its applications to magnetic recording technology. Developing new ways to measure the coupling mechanism between thin magnetic layers through non-magnetic layers is necessary not only for making better sensors and recording media, but also for developing a better theoretical understanding of exchange coupling (direct coupling, biquadratic coupling and indirect coupling like RKKY).

3.5. Spin dynamics and switching

There is a need to understand atomic-scale spin damping in ferromagnetic systems in order to improve the switching speed of magnetic devices. For example, data transfer rates for commercial disk drives must increase to account for the ever-increasing linear bit densities that will require operational bandwidths in excess of 1 GHz in the near future. Similar needs will be required for MRAM as well. One way to understand damping is to investigate size effects as magnetic devices are reduced to sub-micrometer dimensions. For switching times faster than 1 ns, gyromagnetic effects dominate. FMR studies of magnetic nanodots will give a better understanding of spin damping and therefore aid in the development of faster disk drives.

4. Experimental

4.1. Micromechanical magnetometer

The general instrumentation for mechanical measurements of ferromagnetism is shown in figure 1. Typically deflections of the cantilever are measured with an optical detector. Figure 1 shows a laser beam-bounce method, but interferometers can be used with similar performance (see section 4.2). A diode laser source is focused onto the cantilever and reflected into a split photodiode detector. This system is common to many AFM instruments and is capable of detecting 10 pm vibrations under ambient conditions. Microwaves are applied to the sample by placing the cantilever in close proximity to a microstrip resonator driven by a microwave generator. The microwaves are coupled through a $30\,\mu$m wide gap into the resonator from an adjacent microstripline. The resonator and stripline can be fabricated using photolithography on a commercially available epoxy-ceramic compound substrate with a dielectric constant of 9.7 and a loss tangent of 0.003. The resonator with dimensions of 6 mm length and 0.5 mm width has a resonance frequency of 9.15 GHz. An oscillator signal adjusted to match the resonance frequency of the cantilever is used to modulate the microwave field H_1 and is also used as reference for the

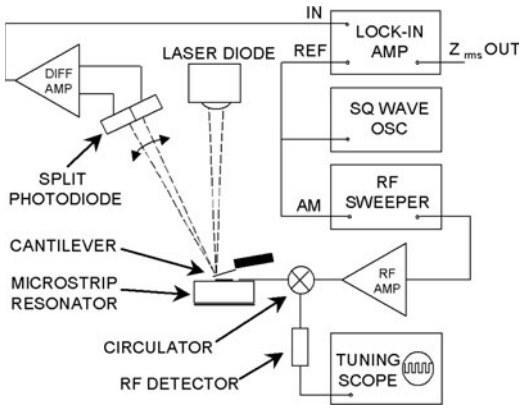

Figure 1. General micromechanical measurement system diagram for magnetometry. The instrument consists of three basic parts: (1) an AFM cantilever detection system, (2) a chopping circuit for modulating electromagnetic fields applied to sample attached to the cantilever, and (3) an rf stripline resonator and tuning circuit for applying microwaves to the sample for FMR spectroscopy measurements.

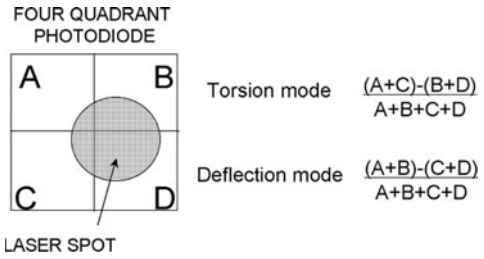

Figure 2. Laser spot on photodiode detector of AFM system. By taking the appropriate difference signals it is possible to measure the cantilever twist as well as deflection.

lock-in amplifier that measures the differences of the outputs from the split photodiode detector. The reflected microwave power from the microstrip resonator is monitored with a tuning scope. The microwave frequency is adjusted to obtain a minimum reflected wave amplitude as measured by the rf diode detector, indicating a maximum coupling of microwave power into the microstrip resonator. The cantilever deflection signal corresponds to the $(C + D) - (A + B)$ signal, whereas the cantilever torque signal corresponds to the $(A + C) - (B + D)$ signal (see figure 2). This configuration enables one to detect both the deflection and the torque signals with the same apparatus. The head of the AFM is non-magnetic and fits into an electromagnet for sweeping field H_0 up to 1.2 T.

4.2. Resonating torque microbalance for in situ *deposition magnetometry*

Figure 3 shows a resonating torque microbalance instrument designed for *in situ* torque magnetometry of magnetic films during deposition. In this instrument an optic-fibre interferometer is used in place of the beam-bounce detector described above to measure the deflection of the cantilever [45]. The cantilever is placed between a pair of SmCo permanent magnets that provide a static bias field H_0 of $10\,\mathrm{kA\,m^{-1}}$. Under these conditions, the film is saturated in plane. A small coil close to the cantilever provides the ac torque

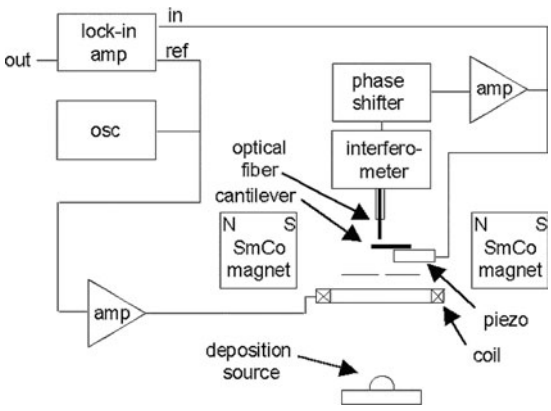

Figure 3. Resonating torque microbalance system diagram for *in situ* thin-film magnetometry. The instrument is similar to that shown in figure 1, with the laser beam bounce detector replaced by an optic-fibre interferometer. A pair of SmCo magnets applies a bias field in the plane of the film deposited onto a mechanical oscillator. Force feedback is used to cancel the magnetic torque applied at the end of the resonator and thus linearize the response of the instrument.

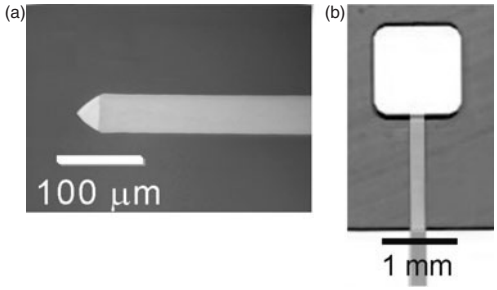

Figure 4. Photomicrographs of Si microcantilevers for magnetometry. (*a*) A lever coated with a permalloy film at the tip. (*b*) A cantilever specially designed for *in situ* deposition magnetometry. The cantilever is physically masked during deposition so that only the substrate is coated. The cantilever is microfabricated from single-crystal silicon and therefore has a very high mechanical Q allowing for better SNR when operated at resonance.

Table 1. Paddle cantilever parameters.

Symbol	Definition	Typical value
a	Magnetic film area	$1\,\mathrm{mm^2}$
l	Cantilever length	$1200\,\mu\mathrm{m}$
w	Cantilever width	25–$200\,\mu\mathrm{m}$
t	Cantilever thickness	19–$27\,\mu\mathrm{m}$
E	Young's modulus	$1.79 \times 10^{11}\,\mathrm{N\,m^{-2}}$
Q	Cantilever quality factor (vacuum)	50 000–200 000

field H_Γ of up to $700\,\mathrm{A\,m^{-1}}$ rms at the resonant frequency of the cantilever. An oscillator supplies the reference signal for a lock-in amplifier as well as current to the coil through a power amplifier. The cantilever deflection signal from the interferometer is phase shifted and amplified, and then applied to the cantilever piezoelectric mount. The phase and magnitude of the piezo signal are adjusted to balance the magnetic torque on the cantilever. This process, referred to as force feedback [46], alleviates resonant-frequency stability problems associated with temperature drift and mass loading effects during deposition. A lock-in amplifier measures the piezo feedback signal, which is proportional to the magnetic moment of the magnetic film.

4.3. Sample preparation

Samples are prepared by depositing films of Co, $Ni_{81}Fe_{19}$ alloy, Ni, Cu, or Au onto single-crystal Si cantilevers. Depositions are done in a diffusion-pump vacuum chamber with a liquid nitrogen-cooled cold trap. The base pressure is 3×10^{-4} Pa. The films are evaporated from alumina-coated tungsten boats at a deposition rate of $0.3\,\mathrm{nm\,s^{-1}}$. Film thickness is measured with a commercial quartz-crystal thickness monitor with a precision of 0.1 nm.

Single-crystal silicon cantilevers and torsional oscillators (described later) were used for the data reported in this paper. The cantilever dimensions are $2.5\mu\mathrm{m} \times 49\,\mu\mathrm{m} \times 449\,\mu\mathrm{m}$ ($\pm 1\,\mu$m), with a deflection spring constant of $0.35\,\mathrm{N\,m^{-1}}$, a deflection resonant frequency of 17 kHz, a torsion spring constant of $3.0 \times 10^{-20}\,\mathrm{N\,m\,rad^{-1}}$, and a torsional resonant frequency of 250 kHz. A series of special paddle shaped

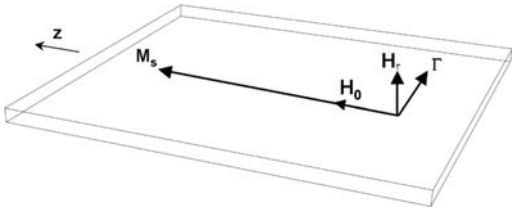

Figure 5. Vector diagram showing the orientations of the magnetic fields and torque on a thin-film magnetized in plane along the z-direction.

cantilevers have been developed for *in situ* magnetometry, as shown in figure 4 [47]. Increasing the area of the magnetic film on the cantilever substrate increases sensitivity to magnetic moment changes per unit of thickness. Typical parameters for these cantilevers are shown in table 1.

5. Results and discussion

5.1. Mechanical torque on a thin magnetic film

The magnetization $\boldsymbol{M}$ in a magnetic film will generate a mechanical torque $\boldsymbol{\Gamma}$ in the presence of an applied torque field $\boldsymbol{H}_\Gamma$ (see figure 5). In many cases, thin-film anisotropy is sufficient to generate mechanical torques that can be measured with micromechanical detectors. In particular, measuring $\boldsymbol{\Gamma}$ allows the determination of the saturation magnetization M_s when a sufficiently large field H_0 is applied in the plane of the film. Given that $\boldsymbol{H}_\Gamma$ is perpendicular to $\boldsymbol{M}_s$, $\Gamma = \mu_0|\boldsymbol{M}_s \times \boldsymbol{H}_\Gamma|V = \mu_0 M_s H_\Gamma V$, where V is the volume of the film. A practical limit for H_Γ is the field strength required to rotate the in-plane magnetization by 5° into the out-of-plane orientation. Below this limit, the in-plane magnetization is within 1% of its value at $H_\Gamma = 0$. The in-plane and out-of-plane anisotropy fields for a given ferromagnetic material and a given geometry determine this field strength. For example, for polycrystalline Fe films thicker than 10 nm, field values on the order of 800 kA m^{-1} are necessary to rotate the magnetization 5° out of plane. For thinner films, this field value can be reduced due to an increase in out-of-plane anisotropy [48]. For a 10 nm thick Fe film, 50 μm wide by 450 μm long, total magnetic moment $m = 2.4 \times 10^{-10}$ A m^2, with $H_\Gamma = 90$ A m^{-1}, we calculate $\Gamma = 2.7 \times 10^{-14}$ N m. In other words, the anisotropy has an equivalent mechanical spring constant that is much larger than the spring constant of the cantilever, so the magnetic moment measurements in this configuration is valid within a few per cent.

We can compute the torque knowing the geometric parameters of the cantilever. For small twist angles θ, $\Gamma = k_\theta \theta$, where k_θ is the torsional spring constant. According to elastic theory [49, 50],

$$k_\theta = \frac{wt^3 E}{6l(1+n)}, \tag{1}$$

where E is Young's modulus, n is Poisson's ratio, t the thickness, w the width, and l the length of the cantilever.

Figure 6 shows the experimental configuration for measuring M–H loops with a microcantilever torque magnetometer [51]. Figure 7 shows two hysteresis loops for 10 nm thick Fe films measured with the instrument and with an AGM for comparison purposes. In this experiment, the

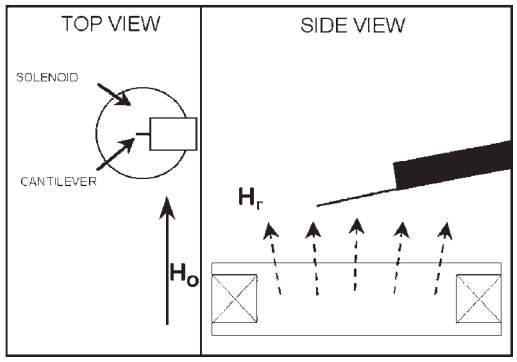

Figure 6. Experimental configuration for measuring M–H loops with a microcantilever torque magnetometer.

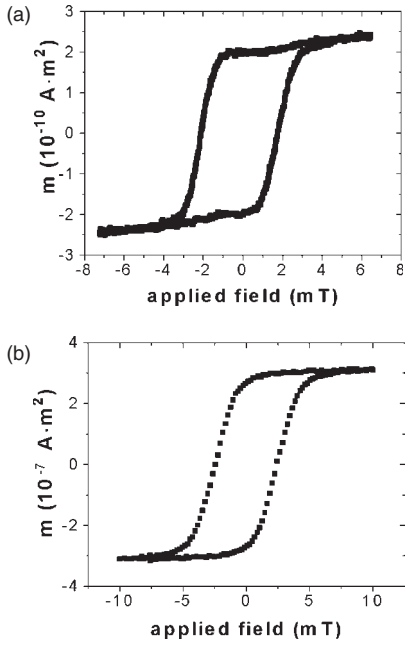

Figure 7. Hysteresis loops for 10 nm Fe films measured with (*a*) the micro-torque magnetometer and (*b*) an AGM.

sweep field H_0 is ramped to the maximum negative value of 7 mT before the data are recorded. The torque field H_Γ provided by the solenoid was kept constant at a level below 0.1 mT for the measurement. These results agree with AGM measurements (see figure 7) performed on films deposited on 6 mm × 6 mm mica substrates placed next to the cantilever substrates. Generally, the characteristic features of the thin Fe films are apparent in both sets of data. The coercivity values, however, are not the same. The AGM measurement shows substantially larger coercivity values. The difference could be explained by structural changes of the Fe film prepared on mica and by the field gradient of the AGM in the direction of the easy axis of the film. For high coercivity films, this field gradient has little effect on their magnetic properties, but for soft magnetic films it will change their magnetic properties. In contrast, torque-field gradients have a smaller effect on our micro-torque magnetometer measurements, because the torque field is in the direction of the hard axis of the film. Also, the torque field gradients are smaller in amplitude; therefore the torque

coercivity measurements may be more accurate than the AGM measurements.

In order to compute the torque from the torsional angle, the geometric parameters of the microcantilever must be determined accurately. The torsion angle θ is 1.35×10^{-6} rad rms for the 10 nm thick Fe sample, since the diode detector has a sensitivity of 344 nm V^{-1} and the torque signal was 1.76 mV rms. The corresponding torque as calculated from geometrical parameters is $\Gamma = 3.9 \times 10^{-14}$ N m. The torque values as derived from the magnetic and geometrical calculations are close, $\Gamma = 2.7 \times 10^{-14}$ N m, compared to $\Gamma = 3.9 \times 10^{-14}$ N m, respectively. The difference may be attributed to uncertainties in the cantilever geometry (especially thickness).

5.2. In situ *deposition measurements*

Figure 8 shows the averaged values of the magnetic moment after deposition increments as a function of the corresponding film thickness t_f . The measurements were taken *in situ* with the instrument described in figure 1. The trend is for the m/t_f ratios to be smaller for films less than 50 nm, becoming vanishingly small for a thickness below 9 nm. Because dead layers can form during the initial stages of deposition, it is not unexpected that the moment should be reduced for films a few nanometres thick. In addition, the film may be forming oxides or clusters. Further study would be required to determine film microstructure in order to differentiate these possibilities. Finally, the film anisotropy may be quite low and thus there would be little torque transferred to the cantilever. The fact that the data for large thickness extrapolate to zero supports the low anisotropy argument.

Figure 9 shows results for a $Ni_{81}Fe_{19}$ film measured with the force feedback at the cantilever resonance frequency (resonating torque microbalance). Dynamic feedback is used to balance the magnetic torque by applying a mechanical force at the base of the cantilever that is just equal but opposite to the magnetic torque. Spurious results are observed for open-loop detection, whereas the dynamic feedback approach minimizes mass loading and temperature dependent elastic modulus effects that change the resonant frequency of the cantilever during deposition. In addition, the closed-loop cantilever response time is greatly reduced. When feedback is used, the effective Q is reduced without sacrificing SNR [52]. The feedback signal is plotted as a function of torque field for a 30 nm thick Permalloy film deposited onto the paddle. The response of the instrument is linear, as expected over the range shown, indicating that torque energy is well below the anisotropy energy of the film. The corresponding noise level for a torque field of 500 A m^{-1} was 0.1% of total signal. We thus derive a magnetic moment thickness sensitivity level of order 0.03 nm $Hz^{-1/2}$ (see inset in figure 9).

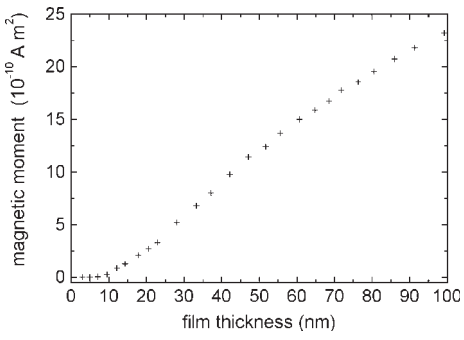

Figure 8. Magnetic moment of a Fe film measured *in situ* with the micro-torque magnetometer versus film thickness measured with a quartz crystal microbalance.

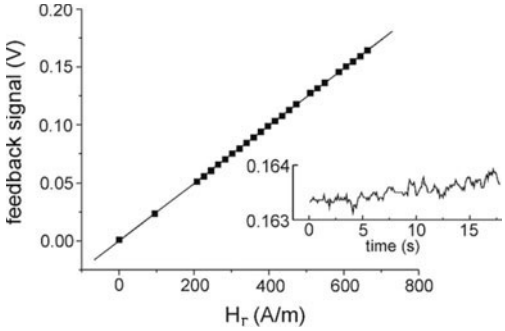

Figure 9. Force feedback signal as a function of torque field for a 30 nm thick NiFe Film. The inset shows the noise level at a fixed torque field as a function of time.

5.3. *Mechanical detection of FMR—general*

The dynamics of the magnetization of a ferromagnet can be described on a phenomenological basis by the Landau–Lifshitz–Gilbert equation [53]

$$\frac{d\boldsymbol{M}}{dt} = \gamma_e(\boldsymbol{M} \times \boldsymbol{H}) + \frac{\alpha}{M_s}\left(\boldsymbol{M} \times \frac{d\boldsymbol{M}}{dt}\right), \qquad (2)$$

where $\boldsymbol{M}$ is the magnetization, $\boldsymbol{H}$ the magnetic field, and γ_e the electronic gyromagnetic ratio. The phenomenological damping factor α is referred to as the Gilbert damping term and is related to the spin–orbit coupling. In a static magnetic field, equation (2) describes a precessional motion of the magnetization decaying from its initial direction until it aligns with the applied field, as shown in figure 10. In a typical FMR experiment, the sample is magnetized by a dc bias field H_0 while a much smaller oscillating field H_1 is applied perpendicular to H_0. FMR occurs when H_0 is adjusted so that H_1 oscillates at the natural precessional frequency of M. The driven FMR response is a continuous precession of the magnetization vector about H_0. The resonant frequency, determined by γ_e and H_0, typically lies in the microwave range. Under FMR conditions, there is a peak in the power absorbed by the magnetic system (inset figure 10).

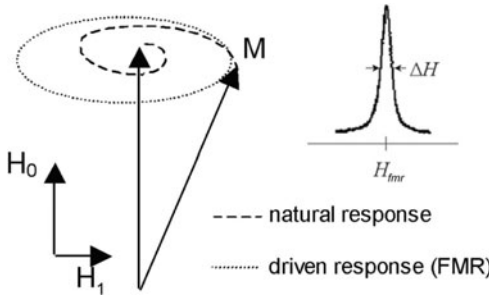

Figure 10. Precession and relaxation of $\boldsymbol{M}$ in response to an applied field $\boldsymbol{H}$.

FMR is generally used to measure the magnetization, but it can also be used as a sensitive probe of other internal fields due to magnetic anisotropy.

The effective saturation magnetization $M_{\rm eff}$, the damping factor α, and the imaginary part of the susceptibility $\chi''_{\rm fmr}$ (at resonance), can be determined from the FMR spectrum using the following relationships for a thin-film sample geometry, in SI units [54, 55]:

$$M_{\rm eff} = \frac{1}{H_{\rm fmr}}\left(\frac{\omega_1^2}{\gamma_{\rm e}^2} - H_{\rm fmr}^2\right), \tag{3}$$

$$\alpha = \frac{\gamma_{\rm e}}{2\omega_1}\Delta H, \tag{4}$$

$$\chi''_{\rm fmr} = \frac{M_{\rm s}}{\alpha}\frac{\gamma_{\rm e}}{\omega_1}\left(\frac{M_{\rm eff} + H_{\rm fmr}}{M_{\rm eff} + 2H_{\rm fmr}}\right). \tag{5}$$

Here, $H_0 = H_{\rm fmr}$ at resonance and ΔH is the width of the resonance peak at half maximum as determined by the Lorentzian fit. Note that $M_{\rm eff} = M_{\rm s} - 8\pi K_{\rm s}/\mu_0 M_{\rm s} t_{\rm f}$, where $M_{\rm s}$ is the saturation magnetization, $t_{\rm f}$ the film thickness, and $K_{\rm s}$ is the uniaxial surface anisotropy energy density parameter [56]. The uniaxial surface anisotropy term $8\pi K_{\rm s}/\mu_0 M_{\rm s} t_{\rm f}$ is about $20\,{\rm kA\,m^{-1}}$ for a polycrystalline 30 nm ferromagnetic film and is negligible to first order compared to $M_{\rm s}$ for these measurements. We therefore assume $M_{\rm eff} = M_{\rm s}$ for the data presented here.

5.4. Mechanical detection of FMR—magnetic moment modulation

The change in the quasi-static mechanical torque under FMR conditions for a thin film is given by

$$\Delta\Gamma_{\rm FMR} = \mu_0 \Delta M_z H_\Gamma V, \tag{6}$$

where ΔM_z is the change in the magnetization due to the FMR precession (see figure 11). For thin magnetic films, M_z can be calculated as [57, 58]

$$M_z = \sqrt{M_{\rm s}^2 - |M_x^2| - |M_y^2|} \approx M_{\rm s} - \frac{|M_x^2| + |M_y^2|}{2M_{\rm s}}, \tag{7}$$

where $M_{\rm s}$ is the saturation magnetization, M_x is the in-plane component of the dynamic magnetization, and M_y is the out-of-plane component of the dynamic magnetization. For $\Delta M_z = M_{\rm s} - M_z$ we see that

$$\Delta M_z = \frac{|M_x^2| + |M_y^2|}{2M_{\rm s}} = \frac{|M_x^2|}{2M_{\rm s}}\left(1 - \left|\frac{M_y}{M_x}\right|^2\right). \tag{8}$$

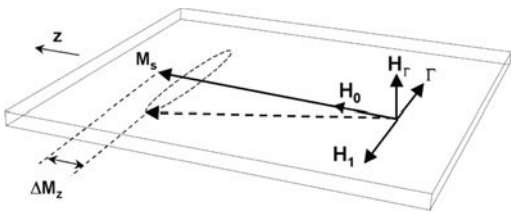

Figure 11. Vector diagram showing the orientation of the applied fields and mechanical torque generated in an FMR experiment.

For a microwave field $H_1 \ll M_{\rm s}$ we can neglect the second term of (8) since the ratio

$$\left|\frac{M_y}{M_x}\right|^2 = \frac{H_1}{H_1 + M_{\rm s}} \ll 1, \tag{9}$$

and so ΔM_z becomes

$$\Delta M_z = \frac{|M_x^2|}{2M_{\rm s}} \approx \frac{(H_1\chi''_{\rm fmr})^2}{4M_{\rm s}}, \tag{10}$$

given that $|M_x| \approx H_1\chi''_{\rm fmr}$ for small FMR tilt angles. It is interesting to note that for magnetic moment modulation FMR spectra the signal is proportional to$(\chi''_{\rm fmr})^2$, compared to conventional spectra, where the signal is proportional to $\chi''_{\rm fmr}$.

The orientation of the cantilever relative to a static torque field H_T from a permanent magnet, the sweep field H_0, and the rf field H_1 is also shown in figure 12. The rf field H_1 amplitude is modulated at the cantilever resonance frequency. The magnetic thin film deposited onto the end of the flat side of the cantilever is saturated by the sweep field H_0 in the plane of the film and 90° relative to the axis of the cantlilever. The microwave field H_1 is not constant throughout the sample. However, it has the proper orientation for FMR, which is perpendicular to H_0 . The static torque in this experiment is not important because the NiFe film is saturated at FMR resonance fields and therefore the static torque adds only a constant offset [59]. The data are shown in figure 13. Note that the direction of the torque is reversed upon reversing sweep field as expected.

With the relations above we can perform a self-consistency calculation. The torque as determined experimentally based on

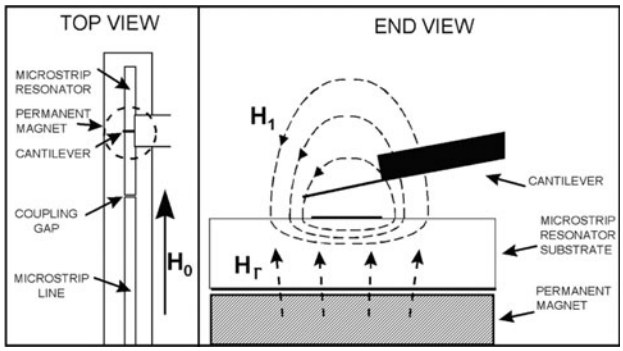

Figure 12. Experimental configuration for FMR with a micro-torque magnetometer.

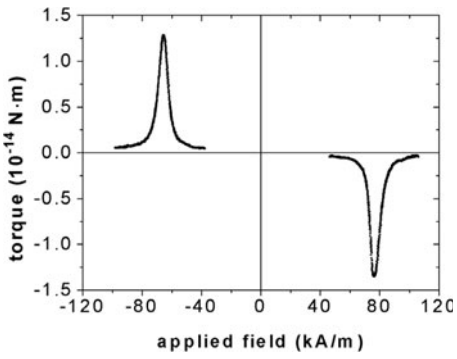

Figure 13. Torque versus applied field measured with the micro-torque magnetometer for a 30 nm thick permalloy film.

cantilever geometrical parameters is $\Gamma_{\rm fmr} = 1.8 \times 10^{-15}$ N m. $\Gamma_{\rm fmr}$ as calculated from our FMR parameters was found to be 1.3×10^{-15} N m, with $M_{\rm s} = 732$ kA m^{-1}, $H_\Gamma = 144$ kA m^{-1}, $H_1 = 53$ A m^{-1} (based on our estimate for a 10 mW microwave input power) and linewidth $\Delta H = 5.7$ kA m^{-1} (based on tuned-cavity FMR measurements of similar samples). The torque values as determined from geometrical parameters and from FMR parameters are in good agreement. The differences between the two calculations for torque are well within the uncertainties associated with our assumptions for calculating ΔM_z, our estimate of ΔH from a tuned cavity FMR spectrometer performed on a similar NiFe film, and our estimate of H_1 that is sensitive to the precise positioning of the cantilever relative to the microstrip resonator [60].

5.5. Mechanical detection of FMR—angular momentum absorption

Damping causes the precessional motion of the magnetization $\boldsymbol{M}$ to lag the oscillating microwave magnetic field $\boldsymbol{H}_1$. A component of $\boldsymbol{M}$ is out of phase with $\boldsymbol{H}_1$ and results in absorption of energy from the microwave field, as discussed above. The component of $\boldsymbol{M}$ that is in phase with and perpendicular to $\boldsymbol{H}_1$ results in a torque. The case shown in figure 14 is for the x-component of $\boldsymbol{H}_1$, h_x, and the rotating $\boldsymbol{M}$ vector. In this case

$$\Gamma_{\rm fmr} = \mu_0 V M_y h_x. \tag{11}$$

Since M_y and h_x are always in phase. In this measurement we do not need a quasistatic torque field H_Γ as discussed above. Rather, the torque is true dynamic torque applied at ω_1.

Spin transitions must conserve energy and angular momentum. Consider the simple case of a gyrotropic material, where a circularly polarized photon with angular momentum $\hbar$ and energy $\hbar\omega$ generates a spin transition. The torque exerted on the system is $\Gamma_{\rm esr} = \hbar\, {\rm d}N/{\rm d}T$ and the power absorbed is $P_{\rm esr} = \hbar\omega_1\, {\rm d}N/{\rm d}T$, where ${\rm d}N/{\rm d}t$ is the number of photons per second absorbed by the sample. Thus we see that $P_{\rm esr} = \omega_1 \Gamma_{\rm esr}$. This is why we refer to this method as 'angular momentum absorption'. However, in the presence of magnetic anisotropies, the elliptical precession of the magnetization allows absorption of different amounts of both left and right circular polarizations for a linearly polarized microwave field. The corresponding transfers of $+\hbar$ and $-\hbar$ angular momenta to the medium partly cancel. Thus, in contrast to ESR and NMR experiments, in which the sample is gyrotropic, the relation $P = \omega_1 \Gamma$ does not hold for FMR experiments, where anisotropy dominates the magnetic response. Instead we have the relationships [61]

$$\Gamma_{\rm fmr} = \frac{\mu_0 M_{\rm s}}{2\alpha(2H_{\rm fmr} + M_{\rm s})} H_1^2 V, \tag{12}$$

$$P_{\rm fmr} = \mu_0 \omega_1 \chi''_{\rm fmr} H_1^2 V = \frac{\mu_0 M_{\rm s} \gamma_{\rm e} (H_{\rm fmr} + M_{\rm s})}{2\alpha(2H_{\rm fmr} + M_{\rm s})} H_1^2 V, \tag{13}$$

and thus

$$\frac{P_{\rm fmr}}{\Gamma_{\rm fmr}} = \gamma_{\rm e}(H_{\rm fmr} + M_{\rm s}) = \frac{\omega_1^2}{\gamma H_{\rm fmr}}. \tag{14}$$

The experimental configuration shown for FMR detection by angular momentum absorption is shown in figure 15. Figure 16 shows the FMR resonance spectra as a function of the bias field for a 30 nm thick $Ni_{81}Fe_{19}$ film. The

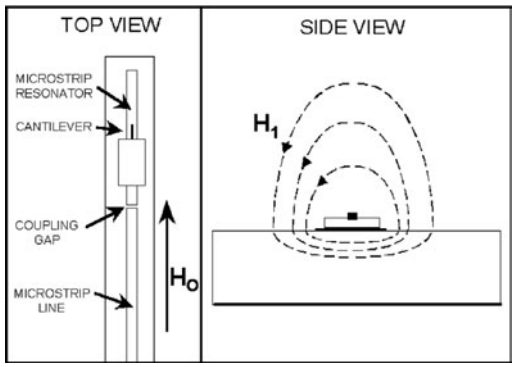

Figure 15. Experimental configuration for FMR by angular-momentum absorption. In this configuration a static torque field is not required for FMR detection. The microwave field itself provides a net time-averaged torque to the sample that twists the cantilever.

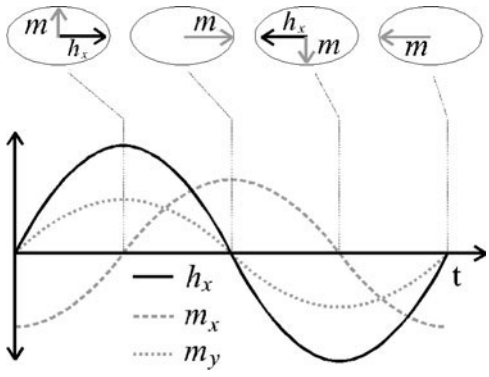

Figure 14. Damping causes the precession of the magnetization m to lag the oscillating microwave magnetic field h_x. A component of m_x is out of phase with h_x and results in absorption of energy from the microwave field. The component of m_y that is in phase with h_x is perpendicular to this field and results in a torque. The case shown here is for a 90° lag, which occurs near resonance.

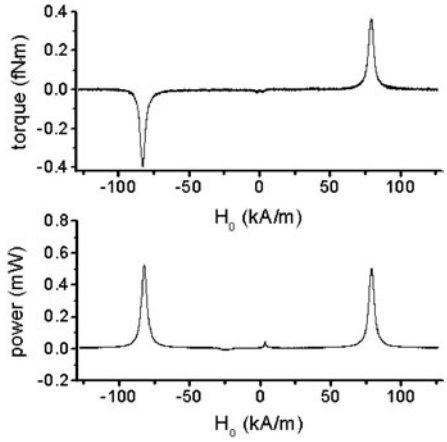

Figure 16. Torque and absorbed power as a function of bias field at a fixed microwave frequency of 9.15 GHz. The top plot is the signal measured from the torsion of the cantilever. The sign of the torque reverses for opposite directions of the bias field. The bottom plot is the signal measured from the deflection of the cantilever.

upper graph shows the torque on the sample as determined from the cantilever torsion. Note that when the bias field is reversed, the torque acts in the opposite direction. The clockwise (or counterclockwise) precession of the spins in the presence of a positive (or negative) bias field produces a clockwise (or counterclockwise) torque along the cantilever axis. The lower graph shows the absorbed power measured by calorimetry (see next section) as determined from the cantilever deflection. This measure is independent of M_s, sample volume, and strength of the microwave field H_1. With $\omega_1/2\pi = 9.15\,\mathrm{GHz}$, $H_{\mathrm{fmr}} = 82.1\,\mathrm{kA\,m^{-1}}$, and $\gamma_e = 2.31 \times 10^5\,\mathrm{m\,A^{-1}\,s^{-1}}$, equation (14) predicts $P_{\mathrm{fmr}}/\Gamma_{\mathrm{fmr}} = 1.74 \times 10^{11}\,\mathrm{Hz}$ at resonance, compared to the experimentally determined value of $8.28 \times 10^{11}\,\mathrm{Hz}$. In this experiment, the power and torque were derived from the estimated mechanical response of the cantilever based on its dimensions and material properties. Uncertainty in these parameters accounts for the deviation from the expected value. Additional structures patterned onto the cantilever would allow for calibration of the P/Γ response.

5.6. Mechanical detection of FMR—bimaterial calorimeter

A bimaterial calorimeter for FMR can be understood within the mathematical framework developed for other bimaterial thermal sensors. Consider the silicon cantilever with a magnetic coating as a rectangular beam fixed at one end composed of two layers that have different thermal properties. Barnes *et al* [62] solve the heat equation for this configuration and show that the deflection at the free end of the beam is

$$z = a\frac{E_1}{E_2}\frac{t_1^2 l^3}{t_2^3 w}\left(\frac{\gamma_1 - \gamma_2}{\lambda_1 t_1 + \lambda_2 t_2}\right)P, \qquad (15)$$

where γ, λ, t, w, l, and E are, respectively, the thermal expansion coefficient, thermal conductivity, thickness, width, length, and Young's modulus of the beam layers (subscripts refer to the different materials), and P is the absorbed power. Equation (15) applies only in the limit $t_1 \ll t_2$ (t_1 is thickness of the magnetic film, and t_2 is the thickness of the silicon cantilever). Note that by definition $t_1 \equiv t_f$ and $t_2 \equiv t$ as discussed above. In addition, it is assumed that the temperature is constant over any cross-section along the axis of the cantilever; this is a good approximation if $t_1, t_2 \ll l$. The constant a ranges from a value of 2 if power is absorbed near the end of the beam, to a value of 1.25 if power is absorbed uniformly along the beam.

There is significant 'off-resonance' microwave absorption for a metallic bimaterial sensor due to eddy-current heating. In these experiments, the skin depth $\delta = (2\rho/\mu\omega_1)^{1/2}$ is about $1\,\mu$m (μ is the permeability of the film and ρ is the electrical conductivity). The ac power loss for a thin metal film scales with ρ when $t_f < \delta$, as is the case here. The surface resistance of a metallic film, assuming that losses are dominated by eddy-current heating, is $Z \approx \rho/t_f$ given $t_f \ll \delta$. This result can be verified based on first principles given that one must further require that the reflectivity of the film be close to unity. As the film thickness is decreased and its reflectivity drops well below unity, the relation $Z \approx \rho/t_f$ is no longer valid [63]. Under these conditions we expect that the offsets of the absorption peaks should scale approximately as ρE_1. Eddy-current heating is reduced significantly if H_1 lies in the plane of the FMR detector film [63].

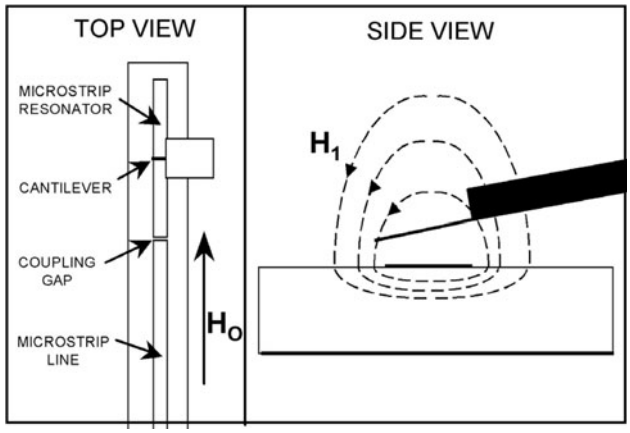

Figure 17. The experimental configuration for FMR with a bimaterial calorimeter.

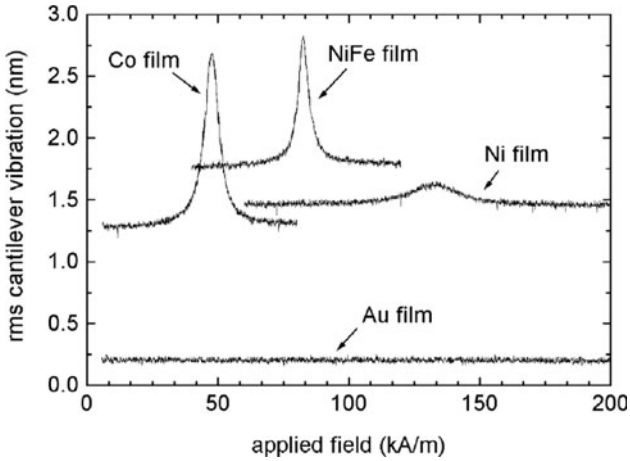

Figure 18. Cantilever vibration versus applied field for several thin-film samples measured with a bimaterial calorimeter. The offsets from zero are due to eddy-current heating of the films.

Table 2. Comparison of FMR data—microwave absorption versus tuned cavity detection.

Sample	H_{fmr} ($\mathrm{kA\,m^{-1}}$)	ΔH ($\mathrm{kA\,m^{-1}}$)	f_1 (GHz)	M_{eff} ($\mathrm{kA\,m^{-1}}$)	α	χ''_{fmr}
Co[a]	47.6	6.8	9.17	1260	0.014	348
Co[b]	60.6	10.4	9.88	1130	0.021	205
NiFe[a]	82.7	5.1	9.17	672	0.010	242
NiFe[b]	93.9	5.7	9.88	676	0.011	219
Ni[a]	132.9	20.0	9.17	334	0.040	26
Ni[b]	154.1	27.4	9.88	326	0.055	18

[a] Microwave absorption. [b] Resonant cavity.
Note: $\gamma_e = 2.31 \times 10^8\,\mathrm{rad\,s^{-1}}\,(\mathrm{kA\,m^{-1}})^{-1}$.

The experimental configuration for FMR with a bimaterial calorimeter is shown in figure 17 [64]. Figure 18 shows the FMR microwave absorption spectra of Co, NiFe, and Ni. The results are shown in table 2. We determined the peak locations and widths by fitting the data to Lorentzian absorption lines. A summary of the FMR data obtained for the same samples with a conventional resonant-cavity spectrometer is shown in table 2 for comparison purposes. Generally, M_{eff}

and α agree for the two types of FMR measurements, but with some differences possibly due to the different detection methods. The resonant cavity FMR spectrometer measures the derivative of the absorption line as a function of field, as opposed to the microwave absorption spectrometer described here, which measures the absorption line directly. In addition, the cantilever chip has several small indentations so that some portions of the magnetic films are at an angle relative to the applied field. This also tends to broaden the FMR line as observed with the resonant-cavity instrument.

6. Magnetic moment sensitivity

6.1. The mechanical thermal limit

The motion of the cantilever due to thermal excitation fundamentally limits its ultimate sensitivity [65]. However, there are several other sources of noise that must be reduced before the thermal motion limit can be achieved. In particular, we have observed substantial noise contributions from the laser diode, the photodiode detector, the microwave source, room vibration, acoustic coupling, and air convection. Operating in vacuum not only reduces viscous damping and thus increases Q but helps decrease acoustic and convective noise sources as well. The Q for bare, single-crystal, silicon cantilevers can be well over 10^4. If the Brownian motion limit can be achieved and we can fabricate coated cantilevers with a Q of 10^4 then it should be possible to improve the sensitivity of MEMS magnetometers significantly. The thermal noise can be expressed in terms of an equivalent noise on the cantilever deflection or torsion. It depends on the spring constant k, the mechanical quality factor Q, the resonant frequency f_0, and the thermal energy $k_B T$. Some typical values for the experiments described in this paper are shown in table 3. Cantilever geometry can be changed to minimize thermal noise. One strategy is to make thin cantilevers with low k [65]. The other is to make small cantilevers with high f_0 [66]. Cantilever geometry, material, and surface coating affect the value of Q. For very thin cantilevers, roughness and surface contamination also become important. Yasumara *et al* [67] have performed a systematic study of these effects on the Q for cantilever deflection modes; however, a study on torsional modes has not yet been done although similar results are expected.

6.2. Comparison of magnetometer magnetic moment sensitivities

Table 4 summarizes reported sensitivities for several types of magnetometers. The conventional systems listed here are for typical instruments designed for routine measurements of relatively large samples. In general, these instruments have larger detectors. One of the main advantages of integrating a sample with a detector, as is the case for the MEMS magnetometers discussed in this paper, is that the sample volume and the detector volume are nearly the same. It is difficult to do this with commercial systems for very small samples. In addition, some commercial systems are not well suited for measurements of low-moment samples because of electronic noise sources or instrument design. For example, a conventional torque magnetometer is very similar to a micro-torque magnetometer in that it measures a mechanical torque due to sample anisotropy when a torque field is applied perpendicular to the surface of the sample. However, for large-sample systems it is difficult to operate in a resonance mode since the mass of the torque arm is quite large compared to the torsion spring constant, making for low resonant frequencies. It is also difficult to physically rotate a large electromagnet quickly.

Other methods have been successfully demonstrated where sample and detector are integrated in a microfrabricated measurement package. Thin films can be deposited directly onto a microstrip transmission line. Microwave transmission can then be measured as a function of applied field. This has been done both inductively as well as using the sample itself as the sensor if it is magnetoresistive. Finally, we refer to work on developing a magnetic resonance force microscope [68] and integrated-sample SQUID magnetometers [69] with the potential for measuring a single-electron spin flip at cryogenic temperatures.

Table 3. Silicon cantilever thermal noise in air.

Deflection	Torque
$F_{\text{noise}} = \sqrt{\frac{2k_B T k}{Q f_0}}$	$\Gamma_{\text{noise}} = \sqrt{\frac{2k_B T k_\theta}{Q f_0}}$
$k = 0.2\,\text{N m}^{-1}$	$k_\theta = 3 \times 10^{-8}\,\text{N m rad}^{-1}$
$f_0 = 15\,\text{kHz}$	$f_0 = 250\,\text{kHz}$
$Q = 200$	$Q = 250$
$F_{\text{noise}} \approx 10^{-14}\,\text{N (Hz)}^{-1/2}$	$\Gamma_{\text{noise}} \approx 10^{-17}\,\text{N m (Hz)}^{-1/2}$

Cantilever dimensions: $l = 499\,\mu\text{m}$, $w = 49\,\mu\text{m}$, $t = 2.5\,\mu\text{m}$.

7. Summary

Figure 19 summarizes the current status of MEMS magnetometers relative to other techniques with some

Table 4. Magnetometer sensitivity comparisons.

Room temperature	A m^{-2}
'Conventional' systems	
Torque magnetometer	10^{-12}
Alternating gradient magnetometer (AGM)	10^{-11}
SQUID magnetometer	10^{-12}
Fluxgate magnetometers	10^{-11}
Vibrating sample magnetometer (VSM)	10^{-9}
FMR spectrometer	10^{-7}
Micromechanical systems	
micro-resonating torque magnetometer	
current status	10^{-16}
predicated	10^{-18}
micro-resonating force magnetometer	
current status	10^{-14}
predicated	10^{-17}
Micromechanical FMR calorimeter	
current status	10^{-12}
predicated	10^{-16}
Other integrated-sample stripline measurements	
inductive	10^{-13}
magnetoresistive sample/sensor	10^{-15}
Cryogenic temperature	
MRFM at 100 mK (predicted)	10^{-23}
1 μm SQUID loop at 4 K (measured)	10^{-21}
0.1 μm SQUID loop at 100 mK (predicted)	10^{-23}

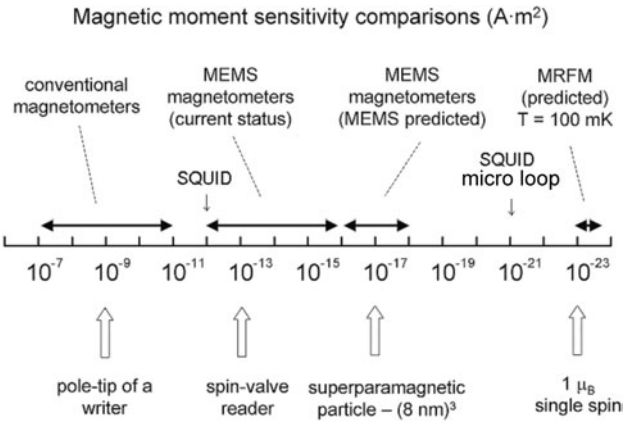

Figure 19. Magnetic moment sensitivity logarithmic scale showing performance benchmarks and comparisons of various kinds of magnetometers.

predictions for ultimate sensitivities. In the figure we show magnetic moment sensitivities on a log scale with benchmarks indicating applications. The term 'conventional magnetometers' refers generally to instruments designed for a larger range of sample size and minimal considerations for small sample-sensor integration. With micromachined sensor optimization we predict sensitivities necessary to study patterned magnetic specimens below the superparamagnetic limit at room temperature. This corresponds to a cube of cobalt 8 nm on a side. The main challenge here is to develop fabrication methods for placing well-defined nanodots onto very sensitive cantilevers. These fabrication methods must be compatible with the micromachining methods used to make the cantilevers. This may be difficult since micromachining involves high-temperature processing and chemically severe etching processes that would harm the nanodot. For smaller particles one must consider lower temperatures to further minimize the thermomechanical noise of the cantilever. In addition, if the particle is superparamagnetic then by definition the anisotropy necessary for quasistatic torque measurements has vanished and other methods based on force gradient magnetometry must be considered. The main challenge here is to generate a known uniform field gradient with sufficient magnitude necessary to detect magnetic forces with a cantilever. As shown in figure 19, there is a large range of relatively unexplored territory below 10^{-12} A m^2 that is now accessible with the microsystems technologies being developed for magnetic measurements.

Contribution of the National Institute of Standards, an agency of the United States Government, not subject to copyright.

References

[1] Taylor B N (ed) 2001 *The International System of Units (SI)* NIST Special Publication 330 (Washington, DC: US Government Printing Office)

[2] Zijlstra H 1987 *Experimental Methods in Magnetism* vol 2 (Amsterdam: North Holland)

[3] Lupien C, Ellman B, Grutter P and Taillefer L 2000 Piezoresistive torque magnetometry below 1 K *Appl. Phys. Lett.* **76** 3564–6

[4] Willemin M, Rossel C, Brugger J, Despont M H, Rothuizen H, Vettiger P, Hofer J and Keller H 1998 Piezoresistive cantilever designed for torque magnetometry *J. Appl. Phys.* **83** 1163–70

[5] Bolle C A, Aksyuk V, Pardo F, Gammel P L, Zeldov E, Bucher E, Boie R, Bishop D J and Nelson D R 1999 Observation of mesoscopic vortex physics using micromechanical oscillators *Nature* **399** 43–6

[6] Harris J G E, Awschalom D D, Matsukura F, Ohno H, Maranowski K D and Gossard A C 1999 Integrated micromechanical cantilever magnetometry of $Ga_{2-x}Mn_xAs$ *Appl. Phys. Lett.* **75** 1140–2

[7] Schwarz M P, Grundler D, Meinel I, Heyn Ch and Heitmann D 1999 Micromechanical cantilever magnetometer with an integrated two-dimensional electron system *Appl. Phys. Lett.* **74** 451–3

[8] Harris J G E, Awschalom D D, Maranowski K D and Gossard A C 2000 Magnetization and dissipation measurements in the quantum Hall regime using an integrated micromechanical magnetometer *J. Appl. Phys.* **87** 5102–5

[9] Judy J W, Yang H, Irazoqui-Pastor P, Yang K, Myung N, Schwartz M and Nobe K 2000 Ferromagnetic micromechanical magnetometers *Tech. Dig. Solid-State Sensor and Actuator Workshop (Hilton Head Island, SC, June 4–8)*

[10] Rossel C, Willemin M, Grasser A, Bothuizen H, Meoijer G I and Keller H 1998 Torsion cantilever as magnetic torque sensor *Rev. Sci. Instrum.* **69** 3199–203

[11] Heydon G P, Farley A N, Hoon S R, Valera M S and Thomlinson S L 1997 Resonant torque magnetometry: a new in-situ technique for determining the magnetic properties of MFM tips *IEEE Trans. Magn.* **33** 4059–61

[12] Biggar R D and Parpia J M 1998 High-Q oscillator torque magnetometer *Rev. Sci. Instrum.* **69** 3558–62

[13] Morrillo J, Su Q, Panchapakesan B, Wuttig M and Novotny D 1998 Micromachined silicon torsional resonator for magnetic anisotropy measurement *Rev. Sci. Instrum.* **69** 3908–12

[14] Barnett S J 1935 Gyromagnetic and electron inertia effects *Rev. Mod. Phys.* **7** 129–66

[15] Peterson L and Ehrenberg A 1985 Highly sensitive Faraday balance for magnetic susceptibility studies of dilute protein solutions *Rev. Sci. Instrum.* **56** 575–80

[16] Flanders P J 1988 An alternating-gradient magnetometer *J. Appl. Phys.* **63** 3940–5

[17] Foner S 1996 The vibrating sample magnetometer: experiences of a volunteer *J. Appl. Phys.* **79** 4740–5

[18] Gibson G A and Schultz S 1991 A high-sensitivity alternating-gradient magnetometer for use in quantifying magnetic force microscopy *J. Appl. Phys.* **69** 5882–90

[19] Todorovic M and Schultz S 1998 Miniature high-sensitivity quartz tuning fork alternating gradient magnetometry *Appl. Phys. Lett.* **73** 3595–7

[20] Aksyuk V, Balakirev F F, Boebinger G S, Gammel P L, Haddon R C and Bishop D J 1998 Micromechanical 'Trampoline' magnetometers for use in large pulsed magnetic fields *Science* **280** 720–2

[21] Binnig G, Quate C F and Gerber Ch 1986 Atomic force microscope *Phys. Rev. Lett.* **56** 930–3

[22] Martin Y and Wickramasinge H K 1987 Magnetic imaging by force microscopy with 1000 Å resolution *Appl. Phys. Lett.* **50** 1455–7

[23] Hug H J, Stiefel B, van Schendel P J A, Moser A, Martin S and Güntherodt H-J 1999 A low temperature ultrahigh vaccum scanning force microscope *Rev. Sci Instrum.* **70** 3625–40

[24] Ascoli C, Baschieri P, Frediani C, Lenci L, Martinelli M, Alzetta G, Celli R M and Pardi L 1996 Micromechanical detection of magnetic resonance by angular momentum absorption *Appl. Phys. Lett.* **69** 3920–2

[25] Arimondo E 1967 Angular momentum detection in magnetic resonance at low fields *Nuovo Cimento* B **52** 379–90

[26] Alzetta G, Arimondo E, Ascoli C and Gozzini A 1967 Paramagnetic resonance detection at low fields with angular momentum detection *Nuovo Cimento* B **52** 392–402

[27] Alzetta G, Arimondo E and Ascoli C 1968 Angular momentum detection of many photon transitions *Nuovo Cimento* B **54** 107–15

[28] Sidles J A, Garbini J L, Bruland K J, Rugar D, Züger O, Hoen S and Yannoni C S 1996 Magnetic resonance force microscopy *Rev. Mod. Phys.* **67** 249–65

[29] Züger O, Hoen S T, Yannoni C S and Rugar D 1996 Three-dimensional imaging with a nuclear magnetic resonance force microscope *J. Appl. Phys.* **79** 1881–4

[30] Rugar D, Yannoni C S and Sidles J A 1992 Mechanical detection of magnetic-resonance *Nature* **360** 563–6

[31] Zhang Z, Hammel P C and Wigen P E 1996 Observation of ferromagnetic resonance in a microscopic sample using magnetic resonance force microscopy *Appl. Phys. Lett.* **68** 2005–7

[32] Moser A and Weller D 1999 Thermal processes and stability of longitudinal magnetic recording media *IEEE Trans. Magn.* **35** 2808–13

[33] Johnson K E 1991 Thin-film recording media: challenges for physics and magnetism in the 1990s *J. Appl. Phys.* **69** 4933–7

[34] Ouchi K 2000 Overview of latest work on perpendicular recording media *IEEE Trans. Magn.* **36** 16–22

[35] Fullerton E E *et al* 2000 Antiferromagnetically coupled magnetic media layers for thermally stable high-density recording *Appl. Phys. Lett.* **77** 3806–8

[36] Sun S, Murray Ch, Weller D, Folks L and Moser A Monodisperse FePt nanoparticles and ferromagnetic FePt nanocrystal superlattices *Science* **287** 1989–92

[37] Puntes V F, Krishnan K M and Alivisatos A P 2001 Colloidal nanocrystal shape and size control: the case of cobalt *Science* **291** 2115–17

[38] Rettner C T, Best M E and Terris B D 2000 Patterning of granular magnetic media with a focused ion beam to produce single-domain islands at >140 Gbit/in^2 *IEEE Trans. Magn.* **37** 1649–51

[39] Tehrani S, Chen E, Durlam M, DeHerrera M, Slaughter J M, Shi J and Kerszykowski G 1999 High density submicron magnetoresistive random access memory *J. Appl. Phys.* **85** 5822–7

[40] Parkin S S P *et al* 1999 Exchange-biased magnetic tunnel junctions and application to nonvolatile magnetic random access memory *J. Appl. Phys.* **85** 5828–33

[41] Bauer G E W, Schmidt G and Molenkamp L W 2002 Elementary magnetoelectronics *IEEE Potentials* **21** 6–10

[42] Jansen R, van 't Erve O M J, Kim S D, Vlutters R, Anil Kumar P S and Lodder J C 2001 The spin-valve transistor: fabrication, characterization, and physics *J. Appl. Phys.* **89** 7431–6

[43] Prinz G and Hathaway K 1995 Magnetoelectronics *Phys. Today* **48** 24–5

[44] Kools J C S 1996 Exchange biased spin valves for magnetic storage *IEEE Trans. Magn.* **32** 3165–84

[45] Rugar D, Mamin H-J and Guethner P 1989 Improved fiber-optic interferometer for atomic force microscopy *Appl. Phys. Lett.* **55** 2588–90

[46] Mertz J, Marti O and Mlynek J 1993 Regulation of a microcantilever response for force feedback *Appl. Phys. Lett.* **62** 2344–6

[47] Moreland J and Hubbard T J 2002 High Q resonating cantilevers for *in situ* measurements of ferromagnetic films *Proc. 2001 Microelectromechanical Systems Conf. (Berkeley)* (Piscataway, NJ: IEEE) pp 36–39

[48] Heinrich B, Arrott A S, Cochran J F, Urquhart K B, Myrtle K, Celinski Z and Zhong Q M 1989 *In-situ* techniques for studying epitaxially grown layers and determining their magnetic properties *Mat. Res. Soc. Symp. Proc.* **151** 177–88

[49] Roark R J and Young W C 1975 *Formulas for Stress and Strain* (New York: McGraw Hill)

[50] Landau L D and Lifshitz E M 1970 *Theory of Elasticity* (New York: Pergamon)

[51] Löhndorf M, Moreland J, Kabos P and Rizzo N 2000 Microcantilever torque magnetometry of thin magnetic films *J. Appl. Phys.* **87** 5995–7

[52] Bruland K J, Garbini J L, Dougherty W M and Sidles J A 1998 Optimal control of ultrasoft cantilevers for force microscopy *J. Appl. Phys.* **83** 3972–7

[53] Heinrich B and Cochran J F 1993 *Adv. Phys.* **42** 523

[54] Chikazumi S 1964 *Physics of Magnetism* (Malabar, Fl: Kreiger) 333–48

[55] Heinrich B and Cochran J F 1993 Ultrathin metallic magnetic films: magnetic anisotropies and exchange interactions *Adv. Phys.* **42** 523–639

[56] Kabos P, Patton C E, Dima M O, Church D B, Stamps R L and Camely R E 1994 Brillouin light scattering on Fe/Cr/Fe thin-film sandwiches *J. Appl. Phys.* **75** 3553–63

[57] Kabos P 1995 *High Frequency Processes in Magnetic Materials* ed G Srinivasan and A Slavin (Singapore: World Scientific) chapter 1

[58] Nash J M, Kabos P, Staudinger R and Patton C E 1998 Phase profiles of microwave magnetic envelope solitons *J. Appl. Phys.* **84** 2689–99

[59] Löhndorf M, Moreland J and Kabos P 2000 Ferromagnetic resonance detection with a torsion mode atomic force microscope *Appl. Phys. Lett.* **76** 1176–8

[60] Jander A, Moreland J and Kabos P 2002 All dielectric micromachnined calorimeter for high resolution microwave power measurement *Technical Digests of the 15th IEEE Int. Conf. Microelectromechanical Systems* pp 635–40

[61] Jander A, Moreland J and Kabos P 2001 Angular momentum and energy transferred through ferromagnetic resonance *Appl. Phys. Lett.* **78** 2348

[62] Barnes J R, Stephenson R J, Woodburn C N, O'Shea S J, Welland M E, Rayment T, Gimzewski J K and Gerber Ch 1994 A femtojoule calorimeter using micromechnaical sensors *Rev. Sci. Instrum.* **65** 3793–8

[63] Booth J National Institute of Standards and Technology Private communication

[64] Moreland J, Löhndorf M, Kabos P and McMichael R D 2000 Ferromagnetic resonance spectroscopy with a micromechanical calorimeter sensor *Rev. Sci. Instrum.* **71** 3099–103

[65] Stowe T D, Yasumura K, Kenny T W, Botkin D, Wago K and Rugar D 1997 Attonewton force detection using ultrathin silicon cantilevers *Appl. Phys. Lett.* **71** 288–90

[66] Lifshitz R and Roukes M L 2000 Thermoelastic damping in micro- and nanomechanical systems *Phys. Rev. B* **61** 5600–9

[67] Yasumara K Y, Stowe T D, Chow E M, Pfafman T, Kenny T W, Stipe B C and Rugar D 2000 Quality factors in micron and submicron thick cantilevers *J. Microelectromech. Syst.* **9** 117–25

[68] Mamin H J and Rugar D 2001 A sub-attonewton force detection at millikelvin temperatures *Appl. Phys. Lett.* **79** 3358–60

[69] Ketchen M *et al* 1993 Octagonal washer dc SQUIDs and integrated susceptometers fabricated in a planarized sub-μm Nb–AlO_x–Nb technology *IEEE Trans. Appl. Supercond.* **3** 1795–9